Fracture mechanisms of aluminium cast alloy locally reinforced by SiC particles and Al_2O_3 whiskers under monotonic and cyclic load

MD. Rafiquzzaman, Y. Arai* and E. Tsuchida

In the present paper, fracture mechanisms and corresponding stress distributions in aluminium cast alloy locally reinforced by SiC particles and Al_2O_3 whiskers under monotonic and cyclic load are investigated experimentally and numerically. The material is monotonically and cyclically deformed to failure at room temperature. The fracture origin and the fracture path are investigated on the fracture surfaces. The fracture occurs in the reinforced part under both monotonic and cyclic loads. Scanning electron microscope (SEM) analysis of fracture surface shows that the fatigue fracture is controlled by the fracture of coarse Al_2O_3 whiskers. The static fracture (monotonic loading) shows that the fracture mechanism is the combination of reinforcing particle fracture and interfacial debonding between reinforcing ceramics and matrix metal. The stress distributions around the boundary between the reinforced part and the unreinforced part are calculated based on an inclusion array model considering the microscopic inhomogeneous effects. Both the experimental results and the finite element simulation show that the critical location for fracture is changed by the external stress level which controls the local stress distribution through plastic constraint between reinforcing particle and matrix alloy.

Keywords: Metal matrix composites (MMCs), Fracture, Fatigue, Fractography

Introduction

In recent years, metal matrix composites (MMCs) have become attractive materials for structural applications such as aerospace, automotive industry and wear applications, especially in the frictional area of braking systems, because of their high strength and stiffness, low density, high temperature properties and excellent wear resistance compared to unreinforced materials.[1] Because of the improved mechanical properties, many researchers have investigated the monotonic and cyclic fracture behaviour and the fracture mechanisms of ceramic particulate/aluminium based MMCs.[2–7] Large differences in strain carrying capability of elastically deforming reinforcement and plastically deforming matrix alloy determine the key mechanism of fracture of MMCs.[2–4,8,9] Owing to constrained plastic flow of the matrix between the reinforcement particles in the MMCs, hydrostatic stresses develop in the matrix which plays an important role in the failure mechanism during monotonic and cyclic deformations.[10,11] Different constraint levels on the matrix flow may control the local failure process (e.g. particle fracture, interfacial debonding and dimple fracture of matrix alloy). Interfacial bonding between reinforcing particles and matrix alloy also tends to be a dominating factor in local failure processes and the strengthening of MMCs. Good interfacial bonding yields high dislocation density in the matrix which increases the strength of MMCs, while low fracture toughness due to cracking of the reinforcing particles is given by good interfacial bonding.[12] Moreover, some studies have focused on the hybrid effect on the mechanical properties of whisker/particle hybrid metal matrix composites.[13–15] Local reinforcement of materials produces lighter components and improves performance in the area required under service conditions. For example, in the brake disc application, ductile aluminium alloy which has high fracture toughness supports the whole disc and the reinforced part by ceramic particles/whiskers is used in the area required (e.g. frictional area).[16] Hybrid (particles and whiskers) preform and squeeze casting are the most common manufacturing methods used to produce partially or locally reinforced materials.[16,17] The resulting strength of the boundary between locally reinforced and unreinforced parts will undoubtedly play an important role in many structural applications. The fracture location and mechanism give critical information of the design or placement of the mechanical component having the locally reinforced part. Under a mechanical loading or temperature change, high stresses occur near the interface edge in the joint of two homogeneous dissimilar materials due to mismatch of material properties (e.g.

Graduate School of Science and Engineering, Saitama University, 255 Shimo-Ohkubo, Sakura-ku, Saitama 338 8570, Japan

*Corresponding author, email yarai@mech.saitama-u.ac.jp

Published by Maney on behalf of the Institute
Received 9 May 2007; accepted 18 July 2007
DOI 10.1179/174328407X239028

thermal and elastic mismatch, plastic flow stress, etc.) of the joined components.[18,19] These high stresses (stress singularity) may influence the fracture of the joint. The stress concentration and influence on the fracture behaviour around the boundary of locally reinforced materials is an unsolved problem. However, locally or partially reinforced materials, especially those reinforced by SiC particles and Al_2O_3 whiskers, have been investigated by a limited number of researchers.[16] Studies of the fracture mechanism, under monotonic and cyclic load, of aluminium cast alloy, locally reinforced by SiC particulates and Al_2O_3 whiskers, are rare. It is believed by the authors that knowledge of monotonic and cyclic fracture behaviours of the locally reinforced aluminium alloy would have an essential role for many structural applications, e.g. in the brake disc of a high speed railway coach.[16]

In the present work, the effects of the boundary between the reinforced unreinforced part on the fracture mechanism, under monotonic and cyclic load, of aluminium cast alloy locally reinforced by SiC particles and Al_2O_3 whiskers, are investigated. Fractographic analysis is used to explain the failure location and the fracture mechanism. The stress and strain distributions predicted by simulations, using a microscopic mechanical model for the locally reinforced materials, are compared to the experimental observations.

Materials and experimental procedures

Hybrid metal matrix composites were fabricated with 21 vol.-%SiC particles and 9 vol.-%Al_2O_3 whiskers as reinforcements and an aluminium alloy of JIS-AC4CH as matrix.[20] The locally reinforced part was fabricated by the squeeze casting process, with a 100 MPa maximum pressure, using a hybrid preform made of SiC particles and Al_2O_3 whiskers. The squeeze casting pressure of 100 MPa is adequate to overcome the resistance against flow and to press the melt into all the open pores of the hybrid preform. Volume fraction and mechanical properties are listed in Table 1. The chemical compositions of AC4CH alloy are listed in Table 2. The specimens were cut out from a locally reinforced aluminium disc shown in Fig. 1. The bend specimen size (width, depth and length) is limited by the limited MMC layer thickness.

The specimens were prepared for the four point bending test, including the boundary between the reinforced part (MMC) and the unreinforced part (aluminium alloy) in the inner span. The machined surfaces of the specimens were hand polished using progressively finer grade (2000 and 3000 grit) of silicon

Table 1 Volume fraction and mechanical properties

Parameter	Al_2O_3	SiC	AC4CH alloy	MMC
Volume content, %	9	21	70	–
Young's modulus, GPa	380	450	70·0	142
Poisson's ratio	0·27	0·20	0·33	0·28
Yield strength, MPa	–	–	131	166

Table 2 Chemical composition of AC4CH alloy, wt-%

Si	Fe	Mg	Ti	Al
7·99	0·2 (max.)	0·57	0·07	Bal.

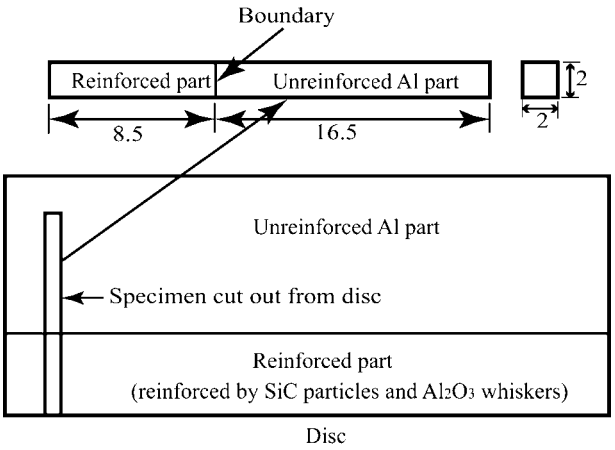

1 Specimen cut out from disc (mm)

carbide impregnated emery paper and then finished with a polishing machine using 1 μm diamond particles until all scratches and surface machining marks were removed. The typical microstructure of the locally reinforced material (AC4CH alloy partially reinforced by SiC particles and Al_2O_3 whiskers) is shown in Fig 2. Most of the SiC particles are rectangular shaped with sharp corners and most of the Al_2O_3 whiskers are roller shaped as shown in Fig. 2*a*. The SiC particles have an average length of 23 μm. The average length and average diameter of the Al_2O_3 whiskers are 33 and 2 μm respectively. In the Al alloy, Al has an average grain size of 48 μm. At frequent intervals a clustering of SiC particles and Al_2O_3 whiskers was observed in the low magnification photograph as shown by the broken line in Fig. 2*b*. The cluster has an average size of 90 μm.

Symmetric four point bending tests were performed using special bending fixtures equipped with a 980 N load cell. The inner and outer span were 10 and 20 mm respectively. Load and deflection data were recorded by a computer data acquisition system. Monotonic bending tests were conducted with a displacement rate of 0·0025 mm s^{-1}. Strength was calculated from the maximum load at failure as a nominal bend stress. Cyclic fatigue tests were also conducted in the load control mode under the load ratio $R=0{\cdot}1$ at frequencies of 1 and 10 Hz. All tests were carried out at room temperature. The number of cycles to failure is taken as the fatigue life N_f. The tensile surfaces of broken specimens were examined with an optical microscope to determine the fracture initiation location. Fractured surfaces were comprehensively examined in a scanning electron microscope (SEM) to determine the microscopic fracture mode and to characterise the microscopic mechanism governing fracture. The microscopic mechanism refers to the local failure processes (fracture of particle or whisker, particle/matrix or whisker/matrix interfacial debonding, dimple fracture of matrix alloy). Energy dispersive X-ray (EDX) analysis was used to identify constituents on the fractured surface. Special effort was made to take matching photographs from the two halves of the broken specimens to assess the relative incidence of particle/whisker cracking and particle/matrix or whisker/matrix interfacial debonding. Additionally, the measured areas of dimple, interfacial debonding and particle/whisker fractures on the fracture

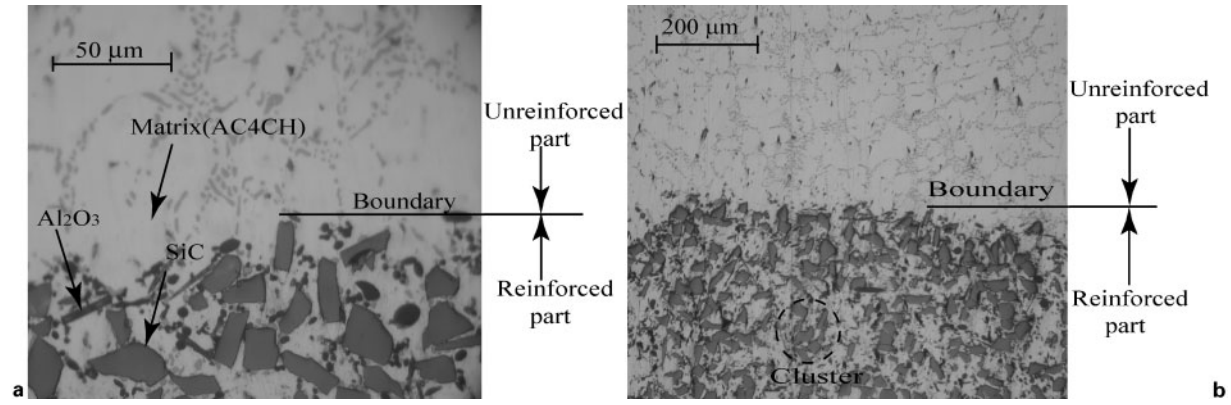

2 Optical microscope photographs of specimen around boundary between reinforced part and unreinforced part

surface were also examined. To determine the area fraction of particle/whisker fractures and interfacial debonding, a particular area with 2 mm in width and 0·05 mm in height parallel and beside the tensile surface has been selected. Therefore, the fraction of the particle and whisker fracture area is defined as the total particle and whisker fracture area divided by the total area measured. The area fractions of particle/matrix or whisker/matrix interfacial debonding were also measured by the same procedure.

Experimental results and discussion

Monotonic test

The nominal bending stress and deflection curves measured by the four point bending test are shown in Fig. 3. The curves exhibit the non-linear relation between nominal bending stress and deflection under stress levels above 200 MPa. The average value of fracture stress is 298 MPa. As indicated in Fig. 4 and Table 3, the fracture of locally reinforced samples occurs at the first or second closest SiC particle to the unreinforced part in the macroscopic boundary between reinforced part (MMC) and unreinforced part (aluminium alloy). The matching halves of the sample fractured as a result of monotonic loading, which include the surface around the fracture initiation site (maximum tension site), are shown in Fig. 5. Fractured particles/whiskers or debonded particles/whiskers are displayed on the fracture surface as well as microscopic dimples of matrix alloy. In Fig. 5, the SiC particle *P* contains a lot of Si (99%) and a small amount of Al (1%) according to EDX analysis. A *P–P* pair in the matching halves, therefore, denotes a SiC particle fracture. The composition *M* contains a lot of Al (92%) and a small amount of Si (8%) which means the area is the Al cast alloy. Therefore, a *P–M* pair in the matching halves denotes SiC particle/matrix interfacial debonding. The composition of the area indicated by *W* contains only Al (100%) which means the area is Al_2O_3. A *W–M* pair in the matching halves, therefore, denotes Al_2O_3 whisker/matrix interfacial debonding and the *W–W* pair in the matching halves denotes Al_2O_3 whisker fracture. The area fractions of particle/whisker fracture and particle/matrix and whisker/matrix interfacial debonding under monotonic and cyclic loading conditions are listed in Table 4. The listed values in monotonic case are the average of the results for specimens TP1, 2 and 3. The area fractions of SiC particle fracture and the interfacial debonding of SiC particle/matrix and Al_2O_3 whisker/matrix are almost the same. From these results, it is clear that the fracture occurred in the particles as well as the particle/matrix interface and Al_2O_3 whiskers/matrix interface under monotonic loading condition. The local

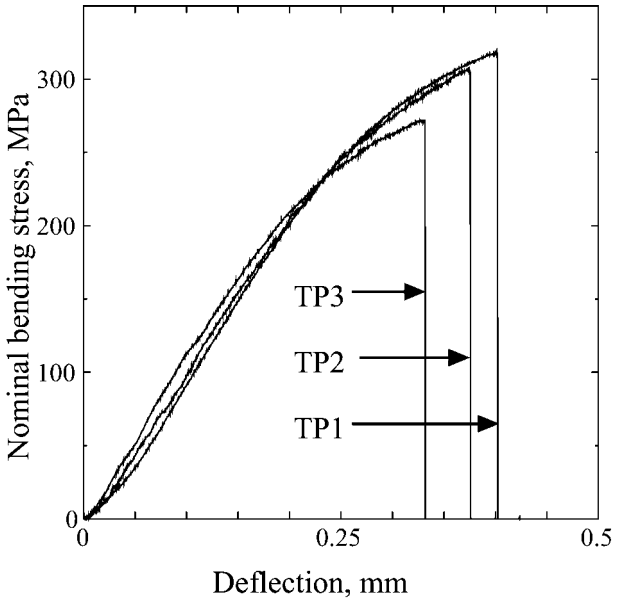

3 Nominal bending stress versus deflection curves under monotonic loading

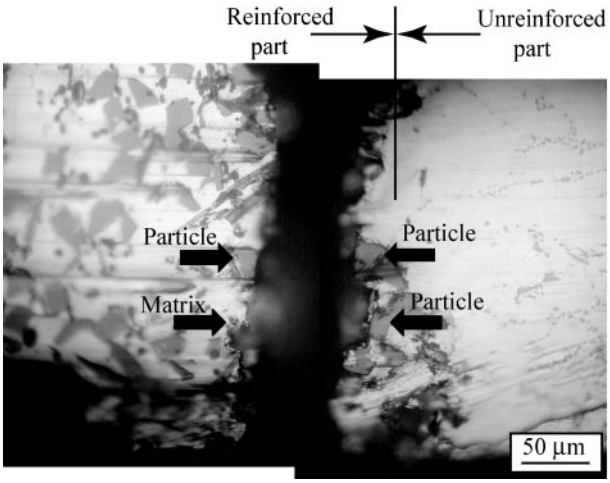

4 Matching surface view of fractured specimen under monotonic loading σ_f=272 MPa

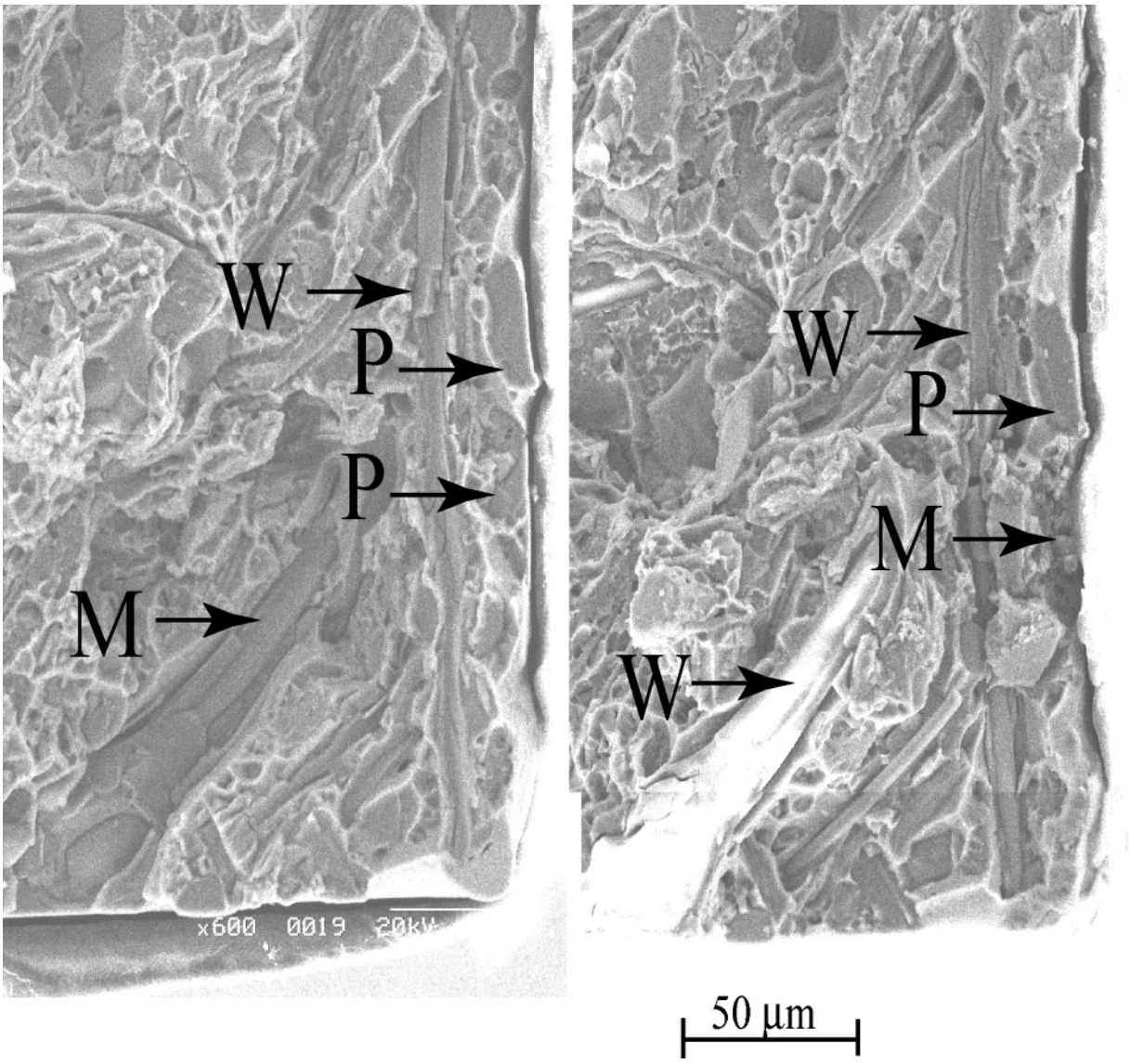

5 Matching fracture surface of locally reinforced material under monotonic loading σ_f=272 MPa

effective stress which is acting on the particle mainly controls the fracture characteristic of reinforcing particles. At the fracture stress under monotonic loading condition, the reinforcing particles and whiskers are deforming elastically within the plastically deforming matrix alloy. Thus, large strain mismatch occurs between these two materials. For this mismatch strain, a consequent concentration of stresses is generated in the particles and whiskers and on the interface between the reinforcing particles/whiskers and matrix alloy. These stresses may cause the separation of particle/whisker and Al matrix alloy or particle/whisker cracking.

Table 3 Fracture stresses and minimum distance from fracture location to macroscopic boundary between reinforced and unreinforced part under monotonic loading

Specimen	Fracture stress, MPa	d_f*, μm
TP1	318	2 particles (46)
TP2	306	1 particle (23)
TP3	272	1 particle (23)

*d_f is the minimum distance from boundary to fracture site.

Fatigue test

The experimental results of fatigue life behaviour of the samples are shown in Fig. 6. The horizontal arrow indicates the test suspended after 10^7 cycles. Fatigue fracture occurs under the maximum stress above one-half of the monotonic fracture stress in the reinforced part. As indicated in Table 5, when the maximum stress is low and the matrix alloy is deformed elastically in the reinforced part, (*see* the results of CTP4–7 in Table 5) the minimum distance of fracture location is far ($0{\cdot}28 \pm 0{\cdot}06$) from the boundary between the reinforced

Table 4 Area fractions of SiC particle and Al_2O_3 whisker fracture and interface debonding between SiC particle matrix and Al_2O_3 whisker matrix under monotonic and cyclic loading condition*

	SiC particle		Al_2O_3 whisker		
Load type	*F*, %	*D*, %	*F*, %	*D*, %	Al (matrix) area, %
Monotonic	10·5	10·1	0·85	9·3	69·25
Cyclic	1·9	19·0	0·85	8·9	69·35

**F* is the fracture area and *D* is the debonding area.

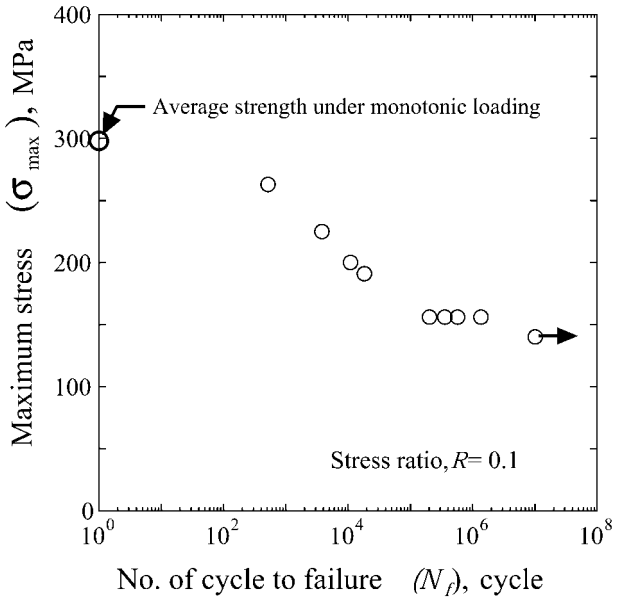

6 Stress versus fatigue life behaviour: stress ratio R=0·1

and unreinforced parts. In the monotonic bending test, the specimens are broken very close to the boundary (i.e. at the first or second particle closest to the unreinforced part, *see* Fig. 4 and Table 3). In the fatigue test, when the maximum stress is high, the specimens are also broken very close to the macroscopic boundary and in the reinforced part (*see* CTP1–3 in Table 5). This occurs when the matrix alloy in the reinforced part is deformed plastically. The difference in the deformation state may be the cause of different fracture locations between the monotonic and cyclic loading. After cyclic tests, the free surface (tension side) of the broken sample was observed in Fig. 7. The cyclic fracture surface around the fatigue crack initiation site is shown in Fig. 8. Figures 7 and 8 are the corresponding tensile surfaces and fracture surfaces respectively. In Figs. 7 and 8, the areas *W* contained a lot of Al (99%) and a small amount of Si (1%) according to EDX analysis. Based on the tensile surface (Fig. 7) and fracture surface morphology (Fig. 8), a *W*–*W* pair in the matching halves can be assigned to a Al_2O_3 whisker fracture. The composition of the area *M* in Figs. 7 and 8 contains a lot of Al (92%) and a small amount of Si (8%). Therefore, the fatigue crack initiates from a coarse Al_2O_3 whisker fracture and propagates through the aluminium alloy matrix. The area fractions of SiC particle/Al_2O_3 whisker fracture and

Table 5 Fatigue life and distance from fatigue fracture location to macroscopic boundary*

Specimen	σ_{max}, MPa	N_f	d_f
CTP1	261	517	2 particles (46 μm)
CTP2	225	3781	0·11 mm
CTP3	200	$1·08 \times 10^4$	0·13 mm
CTP4	191	$1·8 \times 10^4$	0·34 mm
CTP5	156	$5·73 \times 10^5$	0·23 mm
CTP6	156	$3·56 \times 10^5$	0·26 mm
CTP7	156	$2·02 \times 10^5$	0·31 mm
CTP8	156	$1·03 \times 10^6$	0·35 mm

*d_f is the minimum distance from the boundary to fracture site, σ_{max} is the maximum stress and N_f is the number of cycle to failure.

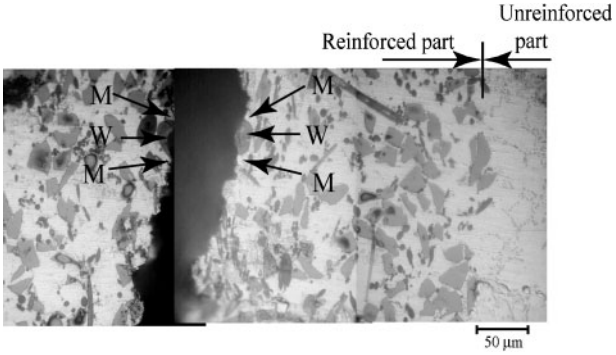

7 Matching surface view of fatigue fractured specimen under cyclic loading: maximum stress σ_{max}=156 MPa; N_f=5·73 × 10^5

interfacial debonding are measured by the same procedure as in the monotonic case and the average value of the results for CTP4 and CTP5 is shown in Table 4. From Table 4, it can be seen that the fracture under the cyclic loading condition is dominated by particle/matrix interfacial debonding and whisker/matrix interfacial debonding. The fracture surfaces of broken specimens under monotonic and cyclic loading conditions show different fracture mechanisms. While the monotonic tests show that the fracture surface is dominated by the combination of particle fracture, particle/matrix interfacial debonding and whisker/matrix interfacial debonding, fatigue tests show that the fracture surface is dominated by particle/matrix interfacial debonding and whisker/matrix interfacial debonding.

Numerical model

In this numerical analysis, two-dimensional modelling was conducted using the finite element method (FEM) to understand the stress distribution near the macroscopic boundary between the reinforced and unreinforced part. Finite element calculations were carried out under the plane strain condition. Figure 9 shows a schematic illustration of a macroscopic model. The reinforced part (MMC) and unreinforced part (Al alloy) are assumed to be homogeneous in the macroscopic model. The boundary between MMC and Al alloy is set at y=0. Elastic properties used in this model are listed in Table 1. To evaluate the elastic constant, yield strength and hardening behaviour of MMC, an infinite periodic circular inclusion array model was used.[4] The yield strength and hardening properties of Al alloy and MMC predicted by the infinite periodic circular inclusion array model are listed in Table 6. The authors use a submodelling concept to consider the effect of microscopic inhomogeneity on the stress field around the boundary between the reinforced and unreinforced part and refer to this model as the 'inclusion array model'. This inclusion array model is shown in Fig. 10. To evaluate the stress concentration in and around reinforced particles and whiskers, a real microstructure in the reinforced part is modelled by an ideal array of circular inclusions. The reinforced part consists of many unit cells and each unit cell includes one circular reinforcement material surrounded by the matrix alloy. The matrix alloy in the reinforced part is of the same composition as the alloy in the unreinforced part. The

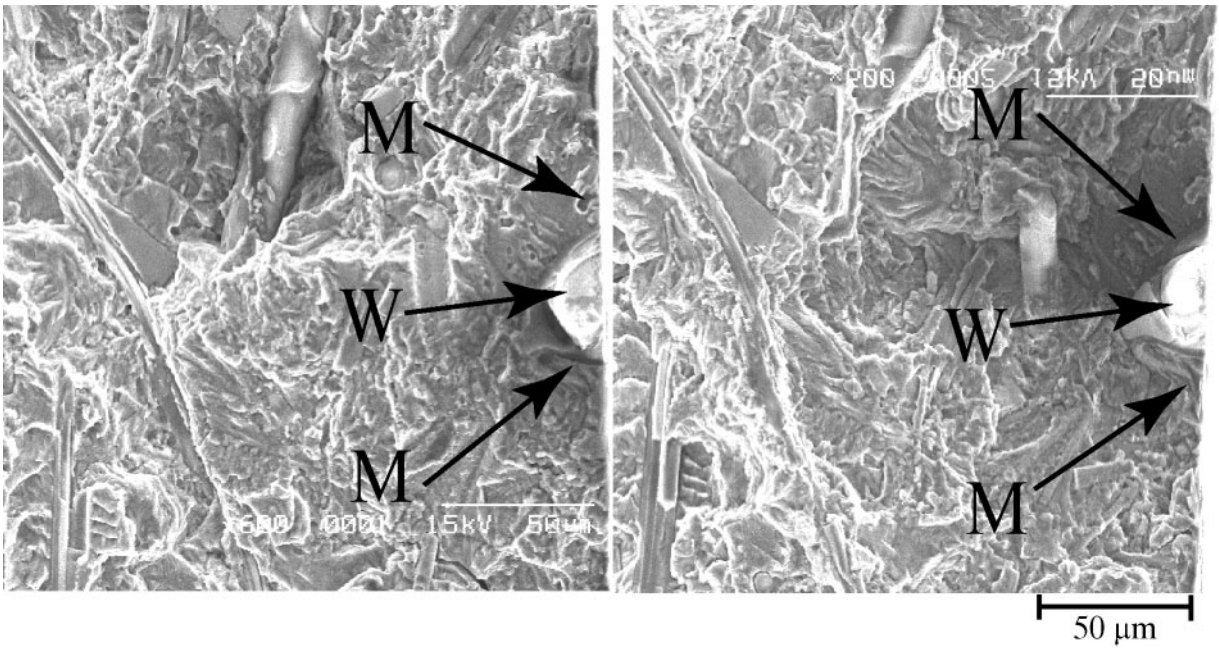

8 Matching fracture surface after fatigue fracture: maximum stress σ_{max}=156 MPa; N_f=5·73×10^5

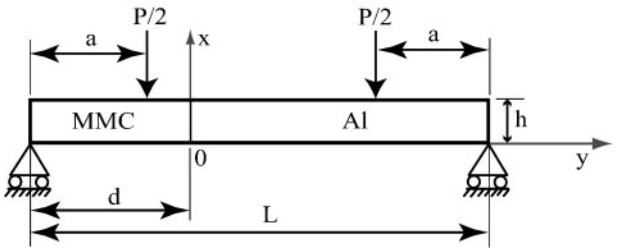

9 Global model of homogeneous materials joint

inclusion array model boundaries

$$\left\{0 \leqslant x \leqslant h_s, y = -\frac{L_s}{2}\right\}$$

$$\left\{0 \leqslant x \leqslant h_s, y = \frac{L_s}{2}\right\}$$

and

$$\left\{x = h_s, -\frac{L_s}{2} \leqslant y \leqslant \frac{L_s}{2}\right\}$$

in Fig. 9 are derived by displacement fields of the macroscopic model results. The non-linear stress–strain relation of AC4CH aluminium alloy was obtained from Ref. 5. The boundary between the inclusion array part and the unreinforced Al part is set at y=0. The model adopted assumes that the circular inclusions only deform elastically while the matrix deforms elastically or elastoplastically depending on the local effective stress level. Geometry of the numerical model is listed in Table 7. As for the fatigue analysis, the predicted results of a loading and an unloading process are discussed. The unloading process is calculated considering the history of the loading process as an initial condition. The difference in total strain between the maximum load state and the fully unloaded state gives the strain amplitude $\Delta\varepsilon_y$ during the cyclic loading. The strain values are taken from the maximum tension side near the free surface and in the matrix. It is evident that the adopted two-dimensional model cannot capture the precise three-dimensional characteristics of the real material quantitatively. However the two-dimensional inclusion array periodic cell model can evaluate the stress distribution at the maximum tension site (maximum stress at particle or interface) and strain amplitude qualitatively.

Numerical results and discussion

To understand the fracture mechanism, two-dimensional stress distributions at the first array of inclusions from the free surface on the tension side are observed. Figure 11*a* shows the distribution under 300 MPa nominal bending stress condition which corresponds to the nominal stress when the specimen breaks under monotonic loading and Fig. 12*a* shows the distribution under the nominal bending stress of 156 MPa which is one of the fatigue tests. Figure 11*b* and Fig. 12*b* show

Table 6 Flow stresses predicted by model

Plastic strain ε_p	Unreinforced part flow stress σ_f, MPa	Reinforced part flow stress σ_f, MPa
0·00	131	166
0·0025	133	185
0·005	137	210
0·0075	139	219
0·001	142	231
0·0015	148	249
0·0017	150	256

Table 7 Geometry of numerical model, mm

Model	L, L_s	h, h_s	a	d	$2r$	$2b$
Global model	20·0	2·0	5·0	7·0	–	–
Inclusion array	1·48	0·444	–	–	0·023	0·037

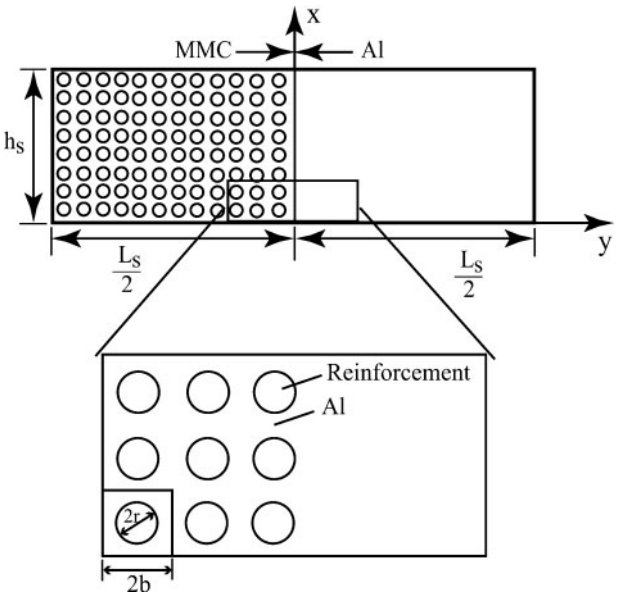

10 Inclusion array model

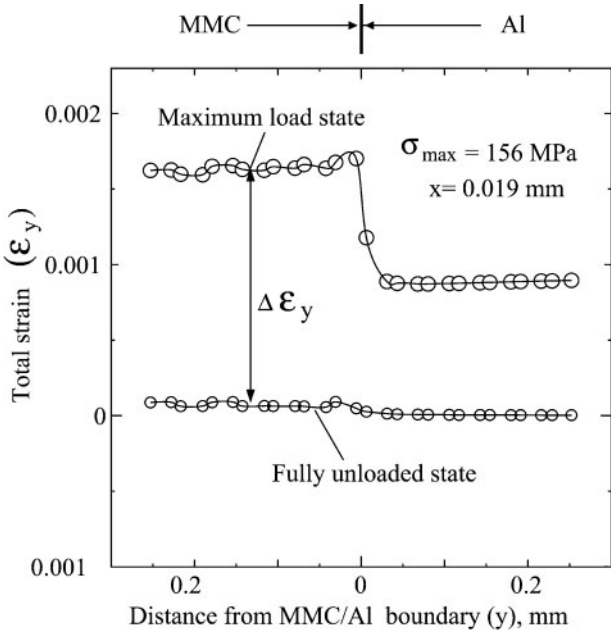

13 Distributions of total strain in matrix along normal to boundary of inclusion array model under cyclic loading at maximum stress 156 MPa

the distribution of the local maximum stress in the each inclusion (square symbol) and the stress on the each interface between particle and matrix (circular symbol). From Fig. 11 it can be seen that the peak stress develops in the first inclusion from the macroscopic boundary between the reinforced part and the unreinforced part (square symbol). The peak stress caused by difference in mechanical properties (e.g. plastic constraint) of the inclusion and matrix leads to the particle fracture because the tensile stress is acting at the inclusion edge (345 MPa) in the high external stress case (Fig. 11*a*). In the experimental observation under the monotonic loading condition, the fracture occurred at the first particle closest to the unreinforced part in the macroscopic boundary. The numerical result, which shows that the peak stress develops in the first inclusion from the macroscopic boundary, is consistent with the fracture location observed experimentally. On the other hand, as shown in Fig. 12, under low nominal bending stress (156 MPa),

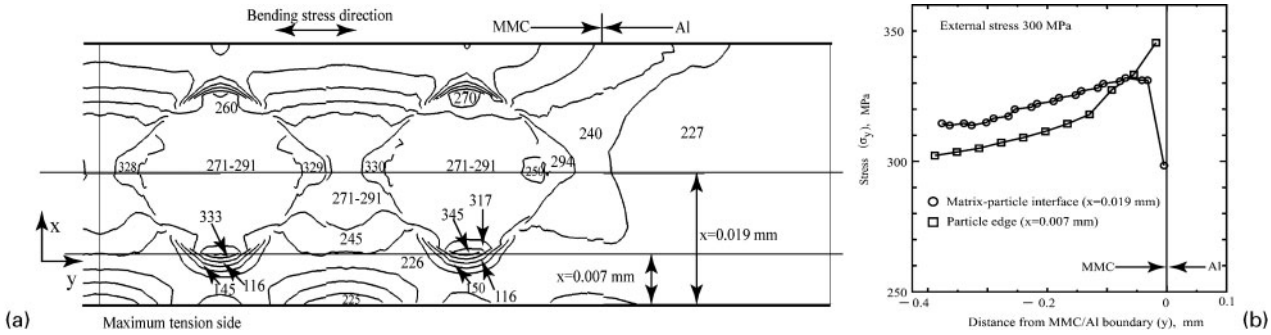

11 Stress distributions along *y* direction of inclusion array model under nominal bending stress 300 MPa

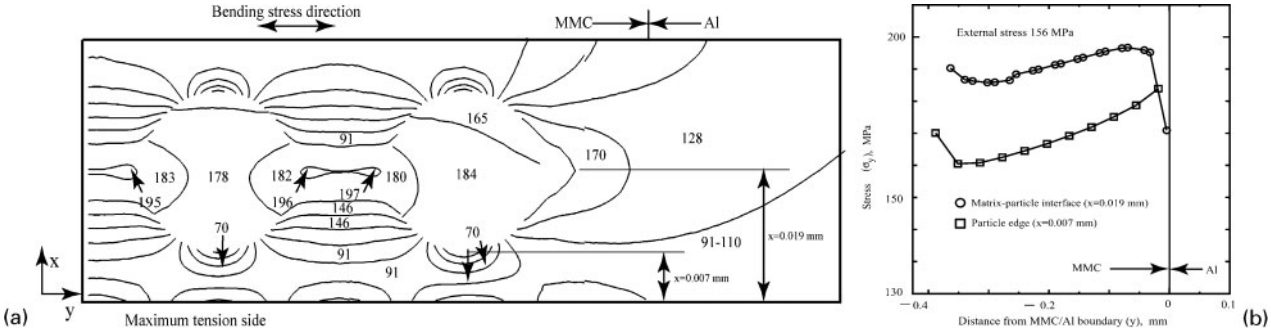

12 Stress distributions along *y* direction of inclusion array model under nominal bending stress 156 MPa

the peak stress develops at the interface between inclusion and matrix (circle symbol) rather than in the inclusion. The maximum tensile stress (197 MPa) acting on the interface also agrees with the fractographic results, thereby, providing further verification of interfacial debonding between the reinforcing materials and the matrix alloy. Distributions of total strain ε_y in the matrix along the normal to the boundary at the maximum load state and the fully unloaded state for nominal bending stress of 156 MPa are shown in Fig. 13. The predicted strain amplitude $\Delta\varepsilon_y$ is much higher in the reinforced side compared to the unreinforced side. In the fatigue test, the specimen fractured in the reinforced part away from the interface. The simulation supports the experimental observation that the fatigue fracture occurred in the reinforced part. Although the monotonic loading also passes the maximum stress, the single monotonic load does not give the unstable failure.

Conclusions

The monotonic and cyclic fracture behaviour of an aluminium cast alloy, locally reinforced by SiC particles and Al_2O_3 whiskers, were investigated experimentally and numerically. The research was concentrated on the fracture mechanism and fracture location of locally reinforced material fractured under monotonic and cyclic loads. The key findings are as follows.

1. The fracture occurs in the reinforced part under both monotonic and cyclic loads.

2. Under cyclic load, the fracture is dominated by interfacial debonding of particle matrix/whisker matrix interfaces, whereas, under monotonic load, the fracture is dominated by both particle fracture and particle/whisker matrix interfacial debonding. The microscopic model gives the consistent maximum stress site which is at the interface between particle and matrix alloy in the low nominal stress case (corresponding to the cyclic load) and at the edge of the particle in the high nominal stress case (corresponding to the monotonic load).

3. Under monotonic load, fracture occurs at the particle closest to the unreinforced part. The numerical result, which shows that the peak stress develops in the first inclusion from the macroscopic boundary, is consistent with the experimentally observed fracture location. As for the fatigue analysis, the predicted strain amplitude in the matrix during cyclic loading is much higher than that in the reinforced part compared to the unreinforced part. This result supports the experimental observation that the fatigue fracture occurs in the reinforced part.

Acknowledgement

The authors thank the Ministry of Education, Science, Sport and Culture, Government of Japan for providing financial support during this research work.

References

1. S. Suresh, A. Mortensen and A. Needleman: 'Fundamentals of metal matrix composites'; 1993, London, Butterworth/Heinemann.
2. M. Levin and B. Karlsson: *Mater. Sci. Technol.*, 1991, **7**, 596–607.
3. D. L. Davidson: *Composites*, 1993, **24**, 248–255.
4. A. L. Chen, Y. Arai and E. Tsuchida: *Theor. Appl. Mech.*, 2004, **53**, 63–73.
5. A. L. Chen, Y. Arai and E. Tsuchida: *Compos. B*, 2005, **36B**, 319–330.
6. T. S. Srivatsan and M. Al-Hajiri: *Compos. B*, 2002, **33B**, 391–404.
7. Q. Zhang, H. Zhang, Gu. Mingyuan and J. Yanping: *Mater. Lett.*, 2004, **58**, 3545–3550.
8. X. Q. Xu and D. F. Watt: *Acta Mater.*, 1996, **44**, 801–811.
9. X. Q. Xu and D. F. Watt: *Acta Mater.*, 1996, **44**, 4501–4511.
10. L. Llorca, S. Suresh and A. Needleman: *Metall. Trans. A*, 1992, **23A**, 919–934.
11. L. Llorca, A. Needleman and S. Suresh: *Acta Metal. Mater.*, 1991, **39**, 2317–2335.
12. R. J. Arsenault and Y. Flom: Proc. Symp. on 'Phase boundary effects on deformation', Toronto, Canada, October 1985, TMS, AIME, 261–279.
13. S. W. Jung, J. H. Lee, J. B. Nam, H. W. Nam and K. S. Han: *Key Eng. Mater.*, 2000, **183–187**, 1297–1302.
14. J. I. Song, S. I. Bae, K. C. Ham and K. S. Han: *Key Eng. Mater.*, 2000, **183–187**, 1267–1272.
15. H. Fu, K. Han and J. Song: *Wear*, 2004, **256**, 705–713.
16. T. Zeuner, P. Stojanov, P. R. Sahm, H. Ruppert and A. Engels: *Mater. Sci. Technol.*, 1998, **14**, 857–863.
17. K. U. Kainer: 'Custom-made materials for automotive and aerospace engineering'; 2006, Weinheim, Wiley-VCH Verlag Gmbh and Co. KGaA.
18. D. B. Bogy: *ASME J. Appl. Mech.*, 1968, **35**, 460–466.
19. B. J. Dalgleish, M. C. Lu and A. G. Evans: *Acta Metal. Mater.*, 1988, **36**, 2029–2035.
20. 'Aluminium alloy castings', JIS H 5202, Japan Industrial Standard 2002.